50C fast-charge Li-ion batteries using graphite anode

Chuangchao Sun

Zhejiang University

Xiao Ji

University of Maryland

Suting Weng

Chinese Academy of Sciences

Li ruhong

Zhejiang University

Xiaoteng Huang

Zhejiang University

Chunnan Zhu

Zhejiang University

Xuezhang Xiao

Zhejiang University

Tao Deng

University of Maryland, College Park

Lixin Chen

Zhejiang University   https://orcid.org/0000-0002-9624-918X

Xuefeng Wang

Institute of Physics, Chinese Academy of Sciences   https://orcid.org/0000-0001-9666-8942

Chunsheng Wang (✉ cswang@umd.edu)

University of Maryland, College Park   https://orcid.org/0000-0002-8626-6381

Xiulin Fan

Zhejiang University

Abstract

Li-ion batteries (LIBs) now have made inroads into the electric vehicle market with high energy densities, yet they still suffer from slow kinetics limited by the graphite anode. Here, we design electrolytes enabling extreme fast charging (XFC) of microsized graphite anode without Li plating. The comprehensive characterizations and simulations on the diffusion of Li+ in the bulk electrolyte, charge-transfer process, and the solid electrolyte interphase (SEI) demonstrate that high ionic conductivity, low desolvation energy of Li+ and protective SEI are essential for XFC. Based on the criterion, two fast-charging electrolytes are designed. Low-voltage 1.8 M LiFSI in 1,3-Dioxolane (DOL) ether electrolyte is for LiFePO4||graphite cells, while high-voltage 1.0 M LiPF6 in a mixture of 4-Fluoroethylene Carbonate (FEC) and Acetonitrile (AN) (7:3 by vol.) is for LiNi0.8Co0.1Mn0.1O2||graphite cells. The former electrolyte enables the graphite electrode to achieve 180 mAh g−1 at 50C (1C=370 mAh g-1), which is 10 times higher than that with conventional electrolyte. The latter electrolyte enables LiNi0.8Co0.1Mn0.1O2||graphite cells (2 mAh cm−2, N/P ratio = 1) to provide a record-breaking reversible capacity of 170 mAh g-1 at 4C charge and 0.3C discharge. This work unveils the key mechanisms for XFC and provides instructive electrolyte design principles for practical fast-charging LIBs with graphite anodes.

Introduction

As the most advanced and portable energy storage devices, lithium-ion batteries (LIBs) have promoted the rapid development of electric vehicles (EVs) over the past few years[1-3]. Compared to the gasoline cars (GCs), the EVs are more environmentally friendly, energy-efficient, and economical. However, one prominent drawback for current EVs is the long wait time for battery charging from the empty to fully charged state, while it only takes a few minutes to fill up the GCs. In this context, "Extreme Fast Charging" (XFC)[4,5] is proposed by the US Department of Energy with the specific requirement of 15-min recharging time (at the rate of 4C) to ensure mass adoption of EVs.

So far, commercial LIBs using graphite anodes and ethylene carbonate (EC)-based electrolytes are impossible to achieve XFC without Li plating because the operating potential of graphite is easily lower to 0 V *vs.* Li/Li$^+$ at high rates[6,7]. A myriad of attempts are dedicated to the structural modification of the graphite to improve the rate performance, such as reducing tortuosity[8] and increasing the porosity[9,10]. However, these attempts to trade high power for low energy density are not suitable for practical applications due to the inevitable reduction in the energy density of batteries. On the other hand, accelerating the Li$^+$ transport process in bulk electrolytes seems to be an efficient way to realize high kinetics[11] without the sacrifice of energy density. Aliphatic esters[12-14] with low viscosity are employed as co-solvents to improve the ionic conductivity (IC), which effectively reduces Li$^+$ transport resistance due to the weak interactions of solvation structures. Ketones, amides[15] and other liquids[16-19] or salts[20-22] have been used as the electrolyte additive to increase the ICs or facilitate the kinetics for Li$^+$ across the interphase[23].

In addition to the above, the recent innovation on battery electrolyte has provided new ideas for fast charging. For instance, high-concentration electrolytes (HCE)[24-26] and localized high concentration electrolytes (LHCEs)[27,28] are able to achieve higher specific capacities of graphite anodes than commercial electrolytes (ICs > 10 mS cm^{-1}) at high rates, despite the relatively low ICs (usually < 5 mS cm^{-1}). Unlike in low-concentration electrolytes (< 2 M), Li$^+$ are transported via repeated "solvation/desolvation" processes in HCEs or LHCEs. The Li-ion desolvation process near the interphase is believed to dominate the kinetics. Thus, reducing the desolvation activation energies (ΔE_{dsv}) of Li$^+$ tends to facilitate the transport of Li ions[29-33] in these electrolyte systems. With the robust SEI derived from anions[34,35], these electrolytes enable a stable cycling performance of graphite anode-based LIBs. Although the currently state-of-the-art study has shown that the graphite can achieve a capability of 280 mAh g^{-1} at 5C[25], there is still a long way to go for XFC. Other endeavor has been made in low-concentration electrolytes with low ΔE_{dsv}[36], regrettably, only introducing mediocre improvements.

Herein, we challenge the traditional consideration of unilaterally improving the rate performance and propose an electrolyte design criterion for high-rate graphite anode-based LIBs. We demonstrate that low desolvation energy of Li$^+$ in electrolyte endows a fast interfacial kinetics, and ultrahigh rate graphite anode with a decent cycling stability can be achieved by simultaneously improving the IC of electrolyte and forming thin but robust SEI. According to the theoretical calculations and experimental results, we formulate 1.8 M LiFSI in 1,3-Dioxolane electrolytes which enable micro-sized natural graphite (NG) electrodes to achieve a long-cycling capacity of 315 mAh g^{-1} at 20C (1C=370 mAh g^{-1}) without capacity decay. Even in 50C, a highly reversible capacity of 180 mAh g^{-1} is retained. The NG electrodes achieve a reversible capacity of 310 mAh g^{-1} after reducing the temperature to -30°C at 0.3C. The 1.8 M LiFSI DOL electrolyte enables LiFePO$_4$(LFP)||graphite cells to achieve a capacity of 60 mAh g^{-1} (of LFP) without decay during long-time cycling along with a stable Coulombic efficiency of 99.99%. To couple with high voltage LiNi$_{0.8}$Mn$_{0.1}$Co$_{0.1}$O$_2$ (NCM811) cathode, a high-voltage fast-charging electrolyte consisting of 1.0 M LiPF$_6$ in 4-Fluoroethylene Carbonate (FEC) and Acetonitrile (AN) (7:3 by vol.) is also designed. Our results demonstrate that 1.0 M LiPF$_6$ in FEC/AN electrolyte enables NCM811||NG cells (cathode loading: 2 mAh cm^{-2}) to deliver a reversible capacity of 170 mAh g^{-1} at 4C charge and 0.3C discharge. The design principle makes XFC promising for practical applications in graphite anode-based LIBs.

Results

Electrolyte design for high-rate graphite anodes. The energy storage rate relies on how fast the Li$^+$ can migrate between the cathode and the anode. In principle, Li$^+$ undergoes three steps during charging processes (Fig. 1a): (a) diffussion of solvated Li$^+$ in the bulk electrolyte, (b) desolvation of the solvated Li$^+$ before crossing the SEI and (c) naked Li$^+$ crossing the SEI[11]. These three steps are highly intertwined. The physicochemical properties of the solvents and concentration determine the diffusivity of the Li$^+$, while the components of the Li$^+$ inner solvation shell affect the SEI compositions and thereby plays a

decisive role in the Li$^+$ crossing kinetics in SEI. Accelerating the Li$^+$ transport in all three steps will dramatically enhance the electrochemical kinetics, which calls for the electrolyte with the high ionic conductivity (IC), low desolvation energy (ΔE_{dsv}) and low Li$^+$ crossing energy-barrier SEI (ΔE_{SEI}) with a low area specific resistance (ASR). To design an electrolyte with these properties, the IC (Fig. 1b), ΔE_{dsv} (Fig. 1c), and reduction potential (G_{red}, Fig. 1d) for the commonly used salts and solvents were firstly measured *via* experiments and DFT calculations (Fig. 1c,d). According to the results, FSI$^-$ anion exhibits the lowest ΔE_{dsv} (Fig. 1c) and highest reduction potential among the anions (Fig. 1d), which indicates that FSI$^-$ anion can endow low desolvation kinetics and inorganic-rich SEI. For the solvents, AN based electrolytes show superior ionic conductivity to enhance the Li$^+$ migration and transport inside the electrolyte (Fig. 1b), while DOL solvent which demonstrates the weakest interaction with Li$^+$ (Fig. 1c) should be a good choice to improve the desolvation kinetics. FEC solvent is favorable for the LiF-rich SEI as it can promote the formation of LiF at around 1.0 V. LiF-rich SEI is very thin and has a low ASR because LiF has a high ratio of ionic conductivity to electronic conductivity. The corresponding Quantum Chemistry calculations of reduction potentials for Li-solvent/anion with different dielectric constants are shown in Supplementary Fig. 1.

We selected LiFSI as the salt because it has the best dissociation and highest potential to form LiF (Fig. 1d) among the studied common salts, and DOL as the solvent for the lowest ΔE_{dsv} of Li$^+$ (Fig. 1c). To maximize the rate performance, 1.8 M LiFSI DOL was blended since the conductivity maxima locates at this concentration (Supplementary Fig. 2b). The correlating solvation structures were examined by Raman spectroscopy (Supplementary Fig. 2c). The C-O-C bending peak ascribed to DOL is slightly perturbed (721 to 730 cm^{-1}) by the dissolution of LiFSI, while the other three C-O stretching peaks of DOL (940, 958 and 1088 cm^{-1}) keep intact[37], implying weak coordination of DOL molecules bound by Li$^+$, *id est*, a low ΔE_{dsv} of Li$^+$ in 1.8 M LiFSI DOL electrolyte.

Molecular dynamics simulation was performed to analyze the detailed solvation structures of the electrolytes (Supplementary Fig. 3). Unlike the strong coordination of Li$^+$ with solvent in 1.0 M LiPF$_6$ EC/DMC electrolyte, Li$^+$ prefers to bond with FSI$^-$ in 1.8 M LiFSI DOL electrolyte as evidenced by a much higher peak of Li-O$_{FSI}$ than that of Li-O$_{DOL}$. The corresponding pie chart (Supplementary Fig. 3d) indicates a low solvent number of 1.26, which means an easier Li$^+$ desolvation process. Besides the electrolytes, the properties of graphites (morphologies and particle sizes) will also affect the rate performance[38]. In current work, the intercalation/deintercalation behaviors of Li$^+$ in different graphites were evaluated *via* Electrochemical Impedance Spectroscopy (EIS) tests under 100% state-of-charge (SOC) to screen a suitable graphite anode (Supplementary Fig. 4). The total resistances (R$_{cell}$) are in the descending order of mesocarbon microbeads (MCMB) > artificial graphite (AG) > natural graphite (NG) in both two electrolytes (Supplementary Fig. 4a,b). Three natural graphites with different average diameters of 2.5, 10 and 15 μm are named as 2.5NG, 10NG and 15NG. With the smallest average diameter, 2.5NG holds the lowest R$_{cell}$ (15 Ω) in 1.8 M LiFSI DOL electrolyte (Supplementary Fig. 4c), which is benificial for a fast kinetics, and

thus is served as the anode material. The morphologies of different graphites were characterized by scanning electron microscopy (SEM), and no defects or cracks that contribute to a capacitive process are obeserved (Supplementary Fig. 5).

The fast kinetics for graphite anodes. The rate performance of microsized natural graphite (2.5NG) was evaluated in different electrolytes between 1.0 V and 0.0 V using a NG||Li half-cell configuration. The referred rate of nC meant a full charge or discharge in $1/n$ h. Compared to the rapid capacity decline starting from 1C in the carbonate electrolyte, NG anode in 1.8 M LiFSI DOL electrolyte yield a revolutionary breakthrough by providing capacities of 315 and 180 mAh g^{-1} even at 20C and 50C (Fig. 2a), respectively. The recoverable capacity of 370 mAh g^{-1} is obtained when the rate returned to 0.2C, indicating no damage to the graphite anode. The corresponding charge/discharge curves from 1C to 50C reveal the intercalation process of Li$^+$ into graphite (Fig. 2b) with three voltage plateaus emerging below ~ 0.2 V at 1C for 1.8 M LiFSI DOL due to the formation of multistage structures of LiC$_x$[25]. However, no potential plateau can be observed for charging/discharging of graphite in commercial carbonate electrolytes (1.0 M LiPF$_6$ EC/DMC) at a high rate (Supplementary Fig. 6a). At a low rate (< 1C), the Li insertion kinetics is quasi-independent of the electrolytes, showing similar voltage profiles in 1.8 M LiFSI DOL and commercial carbonate electrolytes. As the rate increased to 5C and above, significant differences appear between cells with two electrolytes, particularly in voltage profiles. At such high rates, the battery with 1.8 M LiFSI DOL electrolyte shows a more defined potential plateau and a much lower overpotential in comparison with the commercial carbonate electrolyte. Even when the rate increased up to 20C, the potential plateaus are still defined for the cell with 1.8 M LiFSI DOL electrolyte (Fig. 2b, magenta line). Since the rate performance was measured in a two-electrode cell, the total overpotentials are comprised of two parts: overpotentials for graphite anodes and Li metal electrodes. The real overpotentials for graphite anodes (Fig. 2c) were obtained by subtracting Li metal overpotentials in the galvanostatic Li plating/stripping tests from total overpotentials of the above charge/discharge curves (Supplementary Fig. 6c). When C-rate increases from 1C to 50C, the overpotential of graphite electrode in 1.8 M LiFSI DOL electrolyte is from 0.032 to 0.153 V, which is much lower than that in the carbonate electrolytes (from 0.037 to 0.335 V) (Fig. 2c). Considering the narrow voltage gap (~ 0.1 V) between the Li$^+$ intercalation/de-intercalation potential of graphite with Li metal potential, this variation poses a vital impact on the rate performance of graphite anode.

Galvanostatic intermittent titration technique (GITT)[39,40] using a high rate (10C) was performed to gain insights into the overpotentials in lithiation/delithiation processes of graphite electrodes/LiC$_x$. During the lithiation process, a capacity of > 360 mAh g^{-1} is achieved in the 1.8 M FSI DOL electrolyte in contrast to that of 80 mAh g^{-1} in the commercial carbonate electrolyte (Fig. 2d). The representative potential changes in lithiation and relaxation processes at open-circuit in the middle profiles during GITT experiments are shown in the inset. The whole potential rise in the commercial carbonate electrolyte (142 mV) is 4.6 times higher than that in 1.8 M LiFSI DOL electrolyte (31 mV). Similar phenomena were also observed in the delithiation process with overpotentials of 152 mV and 31 mV in the commercial carbonate and 1.8 M LiFSI DOL electrolyte (Supplementary Fig. 7), respectively. The extremely

large overpotential of commercial carbonate electrolyte should be attributed to the high resistance of the interphases and Li$^+$ desolvation[41], which leads to sluggish kinetics. At the same lithiation/delithiation state of graphite, the similar values of equilibrated potentials (61 *vs.* 67 mV, 9.3 *vs.* 12 mV, 3.4 *vs.* 10 mV) in two electrolytes (Supplementary Fig. 7c,d) indicates that the thermodynamic equilibrium state is independent of the electrolyte. Based on the fitting of Nyquist plot, the cell resistance mainly comprises of bulk resistance (R_b), surface layer resistance (R_{sei}) and charge-transfer resistance (R_{ct}) (Fig. 2e)[6,42]. The much lower values of R_{sei} and R_{ct} (9.1 and 4.7 Ω) than those of the carbonate electrolyte (33.2 and 15.1 Ω), quantitatively verified a faster interfacial reaction kinetics in 1.8 M LiFSI DOL electrolyte. The rate performances of graphite electrode in both electrolytes were further investigated *via* cyclic voltammetry (CV) using NG||Li cells (Supplementary Fig. 8). Basically, the graphite electrode in 1.8 M LiFSI DOL electrolyte experiences significantly deintercalation peaks with lower voltages but intercalation peaks with higher voltages than those in carbonate electrolyte from 0.01 to 1 mVs^{-1}, due to faster Li-ion kinetics. The b-values of each peak, from which we can infer the nature of the redox reaction (limited by semi-infinite diffusion or a capacitive process), were obtained *via* mathematic fitting[43–45], denoted as C1−C3 (charge) and D1−D3 (discharge), respectively (Supplementary Fig. 8b,d). Based on the fitting, the b-values obtained from cells in 1.8 M LiFSI DOL electrolyte are higher than those in carbonate electrolyte. Due to the fast kinetics in 1.8 M LiFSI DOL electrolyte, Li$^+$ can easily reach a ready state to diffuse within the graphite, which endows a strong driving force for the Li$^+$ diffusion in the graphite indicated by the large b-values of each redox peak.

The cycling reversibility of 2.5NG in 1.8 M LiFSI DOL and commercial carbonate electrolytes was evaluated at 20C using NG||Li half cells (Fig. 2f). In stark contrast to only 40 mAh g^{-1} for the cell with the carbonate electrolyte, the cell with 1.8 M LiFSI DOL electrolyte presents a highly reversible capacity of 315 mAh g^{-1}. At high current densities, the Li metal electrode have to be replaced every ~ 1000 cycles to eliminate the pernicious impact (high resistance, dendrites, and electrolyte consumption)[46,47]. Due to the surface corrosion of Li electrode, the cell capacity decreases to 180 mAh g^{-1} after 4000 cycles without replacing the Li metal (Supplementary Fig. 9b,c), which can be recovered by replacing Li count electrodes. Different sized NGs in LiFSI-DOL at various concentrations were also evaluated (Supplementary Figs. 10 and 11). As can be seen, the cell comprised of 2.5NG and 1.8 M LiFSI DOL electrolyte displays the best rate performance. To reach a commercial level, NG electrodes with high loadings of 2 mAh cm^{-2} and 3.5 mAh cm^{-2} (Supplementary Fig. 12a) were tested with 1.8 M LiFSI DOL and showed a high reversible capacity of 340 mAh g^{-1} and 325 mAh g^{-1} at 4C respectively. Compared with the state-of-the-art value of 150 mAh g^{-1} (Supplementary Fig. 12b), the high capacity of NG in our work brought a breakthrough for fast-charging battery chemistry.

SEI characterization. X-ray photoelectron spectroscopy (XPS) was performed to identify the chemical composition of the SEI on cycled graphite electrode with various time of Ar$^+$ sputtering. For the SEI formed in carbonate electrolyte (Fig. 3a), both the organic (RCH$_2$OLi, 290.7 eV) and inorganic (Li$_2$CO$_3$, 291.2 eV) species are detected in the C 1s spectra on the top surface. The content of carbon species is

dominated (~ 80%) according to the XPS elemental analysis after 120 s sputtering with Ar^+ (Fig. 3b), indicating most of the SEI components is derived from the EC decomposition. Meanwhile, the relatively weak signals for Li_2CO_3 and other inorganic species (O, C, P) (Supplementary Fig. 13a) during the sputtering process demonstrate the SEI formed in carbonate electrolyte is organic-rich.

Unlike SEI derived from carbonate electrolyte, the SEI of NG in 1.8 M LiFSI DOL electrolyte contains more inorganic (LiO, LiF) species (Fig. 3c,d and Supplementary Fig. 13b). LiF-rich feature can be confirmed by the intensive LiF signals in F 1s spectra (685.9 eV) and the high ratio of F content (~ 18% *vs.* 5% for SEI in carbonate electrolyte) in XPS elemental analysis. It is well known that LiF-rich SEI stabilizes the Li metal[48] and alloy anodes[49], but few has focused on LiF-rich SEI for graphite anode since the organic-rich SEI derived from the carbonate electrolyte sufficiently enables a decent cycling stability. Compared to the organic-rich SEI, the LiF-rich SEI is more promising for a fast kinetics since two or three atomic layers of LiF could block the side reactions thanks to the wide bond gap and high chemical/electrochemical stability[50]. Some other inorganic species contained N and S were also discovered in the SEI due to the decomposition of FSI^- anions (Supplementary Fig. 14). The *ab initio* molecular dynamic (AIMD) simulated atomic SEI structures on the graphite was provided in Fig. 3e and Supplementary Fig. 15. For the carbonate electrolyte, the open-ringed EC, Li_xPF_6, and Li_2CO_3 clusters can be found, validating that the SEI is mainly resulted from the decomposition of EC solvents. For 1.8 M LiFSI DOL electrolyte, LiF and $LiN_xS_yO_z$ clusters are formed at the interface without the capture of DOL decomposition, revealing that LiFSI is much easier to decompose at the interface, consistent with the XPS results. The formed LiF on graphite with low ionic electronic and high interface energy[50] effectively blocks the continuous reaction of electrolytes, thus increasing the Coulombic efficiency.

Cryogenic transmission electron microscopy (cryo-TEM) technique, which can retain the morphology of *in-situ* SEI[51,52], was carried out to analyze the specific structures of the SEI films. The morphologies and elemental components of the SEI are explicated by high-resolution cryo-TEM with the corresponding fast Fourier transform (FFT) pattern (Fig. 3f,j). For the carbonate electrolyte, the generated SEI presents a classic mosaic-type structure with nano-scale Li_2CO_3 (orange and magenta circles) and Li_2O particles (red circles) (Fig. 3g) dispersed into amorphous organic components[53]. However, the main inorganic components of the generated SEI in the 1.8 M LiFSI DOL electrolyte are LiF (yellow circle) and Li_2O (red circles) with a size of 5−10 nm (Fig. 3j, k), which is also confirmed by the results of other SEI regions (Supplementary Fig. 16). Unlike the SEI with thickness of > 40 nm formed in the carbonate electrolyte (Fig. 3g), the SEI derived in 1.8 M LiFSI DOL electrolyte is only 15 nm (Fig. 3k), which is favorable for the fast transport of Li^+ crossing the SEI. On the other hand, the interphase generated in 1.8 M LiFSI DOL electrolyte exhibits a homogeneous laminar structure (Supplementary Fig. 17b) compared to the irregular morphology formed in the carbonate electrolyte (Supplementary Fig. 17a). Since the detective depth of energy dispersive X-ray spectroscopy (EDX) is micrometer-scale, the detected signal reflects the overlap of both SEI and graphite, which leads to a less apparent content for all elements except C. However, we can still infer that the interphase formed in 1.8 M LiFSI DOL electrolyte is more than ten times richer in

inorganic species (2.61 wt.% F and 4.08 wt.% S) (Fig. 3l) than that formed in the carbonate electrolyte (0.15 wt.% F and 0.01 wt.% P) (Fig. 3h) from the relative contents. The interphase formed in 1.8 M LiFSI DOL electrolyte was also identified by ADF STEM and EELS, showing edge enriched distribution of the detected elements (Fig. 3m), which differs from the broad distribution of elements in the carbonate electrolyte (Fig. 3i).

LiFePO$_4$ ||graphite full cells capable of fast charging and low-temperature operation. Ultrafast-charging capability of 1.8 M LiFSI DOL for Li-ion batteries was evaluated using microsized natural graphite anodes and LiFePO$_4$ cathodes with a high loading, although the high loading would challenge the rate performance[54−56]. We first evaluated the cycle stability of 2 mAh cm^{-2} graphite electrodes at different charging C-rate. Notably, the 1.8 M LiFSI DOL electrolyte enables the graphite electrodes to achieve a capacity of 320 mAh g^{-1} at 4C and 150 mAh g^{-1} at 10 C (Fig. 4a) under such high loading condition, in sharp contrast to a capacity of 20 mAh g^{-1} for the carbonate electrolyte at 4C (Fig. 4a). Meanwhile, a significantly improved cycling performance with a high-capacity retention of 250 mAh g^{-1} over 400 cycles is also achieved for 1.8 M LiFSI DOL electrolyte (Supplementary Fig. 18). In this harsh condition, the Li metal electrode has to be replaced by a fresh one at the 180th cycle to ensure that the degradation of the Li metal under a current density of 8 mA cm^{-2} does not affect the cycling performance (Supplementary Fig. 18c). When the rate increased to 8C (16 mA cm^{-2}), the degradation of the Li metal would be more severe, leading to a more noticeable capacity decay (Supplementary Fig. 19). Another tough condition with the lithiation rate of 4C and delithiation rate of 0.3C (Supplementary Fig. 20) was also employed to verify the practical feasibility and a high capacity of 320 mAh g^{-1} was retained over 200 cycles in 1.8 M LiFSI DOL electrolyte.

LIBs deployed at ultra-low temperatures (≤ -30°C) have limited success due to the dramatic capacity drop, which largely limits their practical application in the extreme environments[57,58]. Although some progress has been reported, the utilized cycling protocol was to charge at room temperature and discharge at low temperatures. Worse kinetics of graphite lithiation at low temperatures remains one of most challenges for the LIBs. Therefore, the low-temperature performances of the cells with the designed electrolytes were also evaluated. Compared to the rapid drop for the ICs of 1.0 M LiPF$_6$ EC/DMC (11.59 to 1.11 mS cm^{-1} from 25 to -30 °C), the IC of 1.8 M LiFSI DOL strictly follows the Vogel-Tamman-Fulcher (VTF) empirical Eq. 5[7] and decreases slowly (15.14 to 7.49 mS cm^{-1} from 25 to -30 °C) (Supplementary Fig. 21), showing a great advantage for Li$^+$ transport in bulk electrolyte at low temperatures. Further low-temperature test (Fig. 4b,c), *id est*, cycling at C/3 under gradually decreasing temperatures from 25 to -30 °C, proves the superiority of the electrolyte by showing a capacity of 300 mAh g^{-1} at -30 °C compared with the carbonate electrolyte (no capacity at -30 °C).

LiFePO$_4$ (LFP) cathode was selected to construct full cell due to its high safety, low cost, and stability[59,60]. Preliminary evaluation of the LFP||Li cells shows the advantages of 1.8 M LiFSI DOL electrolyte by presenting a capacity of 90 mAh g^{-1} at 20C, four times higher than that in the carbonate

electrolyte (20 mAh g^{-1}) (Supplementary Figs. 22 and 23). Coin and pouch full LFP||NG cells tests were also conducted to examine the long cycling stability at 20C (Supplementary Fig. 24 and Fig. 4d). As can been seen, the cell with 1.8 M LiFSI DOL electrolyte delivers an initial capacity of 90 mAh g^{-1} and has no capacity decay after 1000 cycles (Supplementary Fig. 24c). The possible Li plating at high charging rate is the key issue restricting the LIB rate performance[61,62]. Both the digital and SEM images demonstrate that no Li plating occurring at any state of charge (SOC) during the fast-charging process (Supplementary Fig. 25), which guarantees the stable long cycling performance of full cells. At 60C (1 min to full charge and discharge respectively), the pouch cell with 1.8 M LiFSI DOL electrolyte exhibits a capacity of 60 mAh g^{-1} without decay during long-time cycling along with a stable Coulombic efficiency of 99.99% (Fig. 4d and Supplementary Fig. 26), which far exceeds the cell performance with the carbonate electrolyte.

Electrolyte design for fast-charging graphite pairing with NCM811. High-voltage NCM811||graphite cells have received much attention because of their high energy density[63]. Following the criterion above, electrolyte with 1.0 M LiPF$_6$ in FEC/AN (7:3 by vol.) was designed for NCM811||graphite cells. Compared to the carbonate electrolyte, 1.0 M LiPF$_6$ FEC/AN exhibits a lower ΔE_{dsv} (31.43 kJ mol^{-1}) and superior ionic conductivities at room temperature (13.22 mS cm^{-1}) (Supplementary Fig. 27a) and low temperature (2.50 mS cm^{-1} at -30 °C) (Supplementary Fig. 27b). The typical Li$^+$ solvation structures with and without anions were presented in Fig. 5a,b. The RDF results demonstrate an average first shell solvation structure of Li(PF$_6$)(FEC)$_3$AN. The FEC solvent and PF$_6$ anions in the solvation shell tend to be reduced to form LiF at the interface while the AN solvent accelerates the Li-ion transport within the electrolyte, thus meeting the requirements of our proposed mechanisms. Detailed solvation structures of 1.0 M LiPF$_6$ FEC/AN are shown in Supplementary Fig. 28.

The 1.0 M LiPF$_6$ FEC/AN electrolyte enables graphite electrode to achieve a higher capacity of 230 mAh g^{-1} at 20C, which is superior to that of carbonate electrolyte (40 mAh g^{-1}) (Fig. 5c and Supplementary Fig. 29a,b). Moreover, the NCM811||NG cell in 1.0 M LiPF$_6$/FEC:AN with the cathode loading of 2 mAh cm^{-2} maintains a highly reversible capacity of 170 mAh g^{-1} under a harsh cycling condition (4C charge 0.3C discharge).

Discussion

Extremely fast-charging LIBs has been developed by rational design of electrolytes with a criterion, which includs low ΔE_{dsv} of Li$^+$, high ICs as well as abilities to form thin and robust SEI on the graphite surfaces. Based on the criterion, two fast-charging electrolytes 1.8 M LiFSI DOL and 1.0 M LiPF$_6$ FEC/AN (7:3 by vol.) were developed. The former electrolyte enabled the graphite electrode to achieve an extremely high capacity of 315 mAh g^{-1} and 180 mAh g^{-1} at 20C and 50C, respectively. XPS and cryo-TEM characterizations suggested a uniform and LiF-rich SEI at the surface of graphite electrode. The NG||Li cells with a ~ 2 mAh cm^{-2} loading exhibited a high capacity of 320 mAh g^{-1} at 4C and 300 mAh g^{-1} at C/3 under − 30 °C. LFP||NG cells showed a capacity of 80 mAh g^{-1} at 20C and the pouch cells

demonstrated a highly reversible capacity of 60 mAh g^{-1} at a rate of 60C (1 min to full charge and discharge respectively). The latter electrolyte enabled NCM811||NG cells with the cathode loadings of 2 mAh cm^{-2} to retain a capacity of 170 mAh g^{-1} at a tough cycling condition (4C charge 0.3C discharge). Our study established a simple and achievable principle on designing electrolytes for fast-charging graphite anode-based LIBs, which was instructive for practical application.

Methods

Materials. Three sets of NG powders (NG, average diameters: 2.5 μm, 10 μm and 15 μm) were provided by Beijing Xinjincheng Science and Trade Co., Ltd. Artificial graphite powders (AG, average particle size: 15 μm) were purchased from BTR Co., Ltd. Mesocarbon microbeads powders (MCMB, average particle size: 15 μm), LiFePO$_4$ powders (LFP, average particle size: 15 μm) and Carbon Black (Super P C45) were received from Hefei Kejing Co., Ltd. Lithium chips with a thickness of 450 μm (Φ = 15.8 mm) were obtained from Tianjin China Energy Lithium Co., Ltd. Polyacrylic acid (PAA, M_v = 450,000) and lithium hydroxide (LiOH, 99.5%) were purchased from Shanghai Aladdin Co., Ltd. Polyvinylidene fluoride (PVDF, HSV900), N-Methyl pyrrolidone (NMP, 99.5%) were purchased from Duoduo Co., Ltd. 1,3-Dioxolane (DOL, 99.8%), Fluoroethylene carbonate (FEC, 99.8%), Acetonitrile (AN, 99.5%), LiFSI (99%) and LiPF$_6$ (99%) were purchased from Changde Dadu New Material Co., Ltd. All the solvents were dried with molecular sieves at least 48 hours to ensure the moisture content was below 20 ppm (titrated by the Karl−Fischer method).

Preparation of electrolyte and electrode. The electrolyte was prepared and stored inside a glovebox filled with high-purity argon (water and oxygen both < 0.01 ppm). 0.748 g LiFSI was dissolved in 2 ml DOL to obtain 1.8 M LiFSI DOL. 0.167 g LiPF$_6$ was dissolved in 1 ml FEC:AN (7:3 by vol.) mixture to obtain 1.0 M LiPF$_6$ FEC/AN. The carbonate electrolyte was used as the control. The anodes were prepared by casting the mixture containing 80 wt.% graphite, 10 wt.% Carbon Black and 10 wt.% PAALi in deionized water onto a Cu foil current collector using a doctor blade. For the cathode, the mixture of 80 wt.% LiFePO$_4$, 10 wt.% Carbon Black and 10 wt.% PAALi in deionized water was casted onto an Al foil current collector. As for NCM811 cathode, the mixture of 80 wt.% NCM811, 10 wt.% Carbon Black and 10 wt.% PVDF in NMP was casted onto an Al foil current collector. The prepared electrodes were dried at 80 °C for 2 h and further dried under vacuum at 100 °C for at least 12 h before use. The loading of the prepared electrodes was about 0.3 mAh cm^{-2}. For the LFP||NG pouch cells, the N/P ratio is fixed at 1 and the loading of LFP cathode is 1 mAh cm^{-2}. To prepare the electrode with a higher loading about 2 mAh cm^{-2}, the mixture containing 85 wt.% active material, 10 wt.% Carbon Black and 5 wt.% PVDF in NMP was used.

Electrochemical measurements. The ionic conductivities of different electrolytes were investigated by the EIS test using two fixed Pt electrodes. The NG||Li, LFP||Li, LFP||NG and NCM811||NG cells were assembled in 2025-type coin cells using a polyethylene separator (ND16, SK Innovation Co.). The adding electrolyte in each coin cell was about 120 μl to make sure the separator and electrodes fully wetted. Pouch cells were also assembled with different electrolytes for further test. The CV tests were conducted

from 0.01 to 1 V (vs. Li/Li$^+$) at different scanning rates of 0.01, 0.05, 0.10, 0.50 and 1.00 mV s^{-1}. The EIS measurements were performed at the fully discharged state of NG||Li cells with the amplitude of 10 mV over the frequency from 0.01 Hz to 10^6 Hz. All the measurements above were conducted on a multichannel electrochemical analyzer (ivium-n-stat, Ivium Technologies BV Co.). Galvanostatic charge–discharge cycling and rate performances were conducted on a battery test station (Wuhan LAND Electronics Co., Ltd.) at 25 °C.

Characterization. SEM measurements were performed on the pristine graphite particles with a Hitachi SU-70 microscope at 3 kV. For postmortem analyses, NG||Li cells after 5 charge–discharge cycles at 0.2C were disassembled in the glovebox to collect the graphite electrodes. XPS measurements were conducted on a Thermo Scientific ESCALAB 250Xi scanning X-ray microprobe with a monochromatic Al Kα X-ray (1,486.6 eV) source. The samples were etched by Ar$^+$ ions (2 kV, 2 μA, 45° incident angle) with increasing the sputtering time (0 s, 120 s, 300 s, 600 s, 900 s and 1500 s) before the measurements. Cryo-TEM measurements were conducted on a JEOL JEM-ARM200 aberration-corrected microscope at 200 kV. The specimens were first collected on the Cu grids by dispersing the graphite particles in the corresponding solvent, which was operated in a glovebox. Then the specimens were immediately transferred into the TEM column in vacuum under the flow of Ar. Liquid nitrogen poured into the cryo-TEM holder to cool the specimens below – 170°C, at which temperature the specimens were observed.

Quantum chemistry calculations. All quantum chemistry calculations were performed using the Gaussian 09 package. The calculated species included AN, DME, EC/DMC, DOL, TMP, FEC, DEC, TMS, FSI$^-$, TFSI$^-$ and PF6$^-$. The geometries of Li-solvent (anion) complexes were firstly optimized using the B3LYP functional in combination with 6−31 + G(d, p) basis sets. All the optimized structures were confirmed as potential minima, with no frequency modes with imaginary eigenvalues, through frequency analyses following geometry optimizations. The different dielectric constants (*epsl*) represent the different electrolyte with acetone (*epsl* = 20.49) for carbonate-based electrolyte, THF (*epsl* = 7.19) for ether-based electrolyte and diethyl ether (*epsl* = 4.24) for the lower dielectric constant at the interface. The de-solvation energies for complexes (E_{dsv}) were evaluated as the energy difference as follows:

$$G_{dsv} = G_{Li\text{-}Solvent} - G_{Li} - G_{Solvent} \quad (1)$$

where $G_{Li-Solvent}$, G_{Li}, and $G_{Solvent}$ are the Gibbs free energies of the free Li$^+$ ions, free solvent, and complex, respectively. All free energies were evaluated using M05-2X functional with 6−31 + + G(d, p) basis sets.

The reduction potentials versus Li$^+$/Li for various solvents and anions (TFSI$^-$, FSI$^-$ and PF$_6^-$) were predicted using quantum chemistry calculations by subtracting 1.4 V from the absolute reduction potentials, as given in Eq. (2)[64]:

$$E_{red}(M) = -\left[\Delta G_e + \Delta G_S\left(M^-\right) - \Delta G_S(M) \right] / F \quad (2)$$

In the equations, ΔG_e is the or electron affinity in the gas phase at room temperature (298.15 K), $\Delta G_S(M)$ and $\Delta G_S(M^-)$ are the Gibbs free energies of solvation for the M and M^- complexes, respectively, and F is the Faraday constant. M05-2X density functional was adopted because it precisely predicts electron affinity and ionization potential.

Solvation structure simulations. Molecular dynamics (MD) simulations were performed in LAMMPS using the all-atom optimized potentials for liquid simulations (OPLS-AA) force-field with the Li^+, PF_6^- and FSI^- anions description from previous publications[65,66]. The electrolyte systems were setup initially with the salt and solvent molecules distributed in the simulation boxes using Moltemplate (http://www.moltemplate.org/). For each system, an initial energy minimization at 0 K (energy and force tolerances of 10^{-5}) was performed to obtain the ground-state structure. After this, the system was slowly heated from 0 K to room temperature (298 K) at constant volume over 0.2 ns using a Langevin thermostat, with a damping parameter of 100 ps. The system was equilibrated in the constant temperature (298 K), constant pressure (1 bar) (NpT ensemble) for 5 ns before finally being subjected to 5 ns of constant volume, constant temperature dynamics. Radial distribution functions were obtained using the Visual Molecular Dynamics (VMD) software. Snapshots of the most probable solvation shells were also sampled from the simulation trajectory using VESTA.

AIMD calculations. The ab initio molecular dynamics (AIMD) calculations were employed using Vienna ab initio simulation package (VASP) code. Exchange-correlation potentials were parameterized using the generalized gradient approximation (GGA) employing the functional of Perdew-Burke-Ernzerhof (PBE). The projector augmented wave (PAW) approach was used to represent the core electrons and a kinetic energy cutoff of 450 eV was chosen to expand the mono-electronic states in plane waves. The long-range dispersion was accounted for using the DFT-D3 corrections. Because of the large size of the cells, only the *Gamma* point in the reciprocal space was used in our calculations. We applied tritium masses for all protons to allow Born−Oppenheimer dynamics time steps of 1 fs, and a 1×10^{-6} eV energy convergence criterion. The anode is comprised of two layers of fully discharged graphite (LiC_6) with an arm-chair edge. Carbon arm-chair edges were functionalized with either all oxygens. Two electrolyte systems, 1.8 M LiFSI DOL (2 LiFSI and 14 DOL molecules) and 1M $LiPF_6$ EC/DMC (2 $LiPF_6$, 14 EC, and 10 DMC molecules) were tested in this work. Initial geometries of the electrolyte were created with PACKMOL and then quenched using density functional forces. AIMD simulations were then performed at an elevated temperature of 350 K using a Nose thermostat to allow fast equilibration. At least 10 ps of dynamic simulations were performed for each system studied.

Declarations

Data availability

The authors declare that the data supporting the findings of this study are available within the article and its Supplementary Information files.

Acknowledgements

Author contributions

C.S., X.J. and S.W. contributed equally to this work. C.S., C.W. and X.F. conceived the idea for the project. C.S., R.L., X.X., and T.D. prepared the materials and performed the electrochemical experiments. X.J. conducted the QC calculations and MD simulations. S.W. and X. W. performed the cryo-TEM and EELS measurements. X.H. and L.C. conducted the XPS measurements. C.Z. performed the Raman measurements. C.S., X.J. and S.W. drafted the manuscript. C.S., X.W., C.W. and X.F. revised the manuscript.

Competing interests: There are no conflicts to declare.

References

1. Larcher, D. & Tarascon, J. M. Towards greener and more sustainable batteries for electrical energy storage. Nat. Chem. **7**, 19–29 (2015).
2. Chen, R., Li, Q., Yu, X., Chen, L. & Li, H. Approaching practically accessible solid-state batteries: stability issues related to solid electrolytes and interfaces. Chem. Rev. **120**, 6820–6877 (2020).
3. Kim, U.-H. et al. Microstructure engineered Ni-rich layered cathode for electric vehicle batteries. Adv. Energy Mater. **11**, 2100884 (2021).
4. Logan, E. R. & Dahn, J. R. Electrolyte design for fast-charging Li-ion batteries. Trends Chem. **2**, 354–366 (2020).
5. Ahmed, S. et al. Enabling fast charging - a battery technology gap assessment. J. Power Sources **367**, 250–262 (2017).
6. Zhang, S. S. Challenges and strategies for fast charge of Li-ion batteries. Chemelectrochem **7**, 3569–3577 (2020).
7. Burns, J. C., Stevens, D. A. & Dahn, J. R. In-situ detection of lithium plating using high precision coulometry. J. Electrochem. Soc. **162**, A959-A964 (2015).
8. Billaud, J., Bouville, F., Magrini, T., Villevieille, C. & Studart, A. R. Magnetically aligned graphite electrodes for high-rate performance Li-ion batteries. Nat. Energy **1**, 1–6 (2016).
9. Habedank, J. B., Kriegler, J. & Zaeh, M. F. Enhanced fast charging and reduced lithium-plating by laser-structured anodes for lithium-ion batteries. J. Electrochem. Soc. **166**, A3940-A3949 (2019).

10. Lim, S. et al. Improvement of rate capability by graphite foam anode for Li secondary batteries. J. Power Sources **355**, 164–170 (2017).

11. Zhang, S. S. Design aspects of electrolytes for fast charge of Li-ion batteries. InfoMat **3**, 125–130 (2021).

12. Smart, M. C. et al. Improved low-temperature performance of lithium-ion cells with quaternary carbonate-based electrolytes. J. Power Sources **119**, 349–358 (2003).

13. Smart, M. C., Ratnakumar, B. V., Chin, K. B. & Whitcanack, L. D. Lithium-ion electrolytes containing ester cosolvents for improved low temperature performance. J. Electrochem. Soc. **157**, A1361-A1374 (2010).

14. Smart, M. C., Lucht, B. L., Dalavi, S., Krause, F. C. & Ratnakumar, B. V. The effect of additives upon the performance of MCMB/LiNi$_x$Co$_{1-x}$O$_2$ Li-ion cells containing methyl butyrate-based wide operating temperature range electrolytes. J. Electrochem. Soc. **159**, A739-A751 (2012).

15. Hall, D. S. et al. Exploring classes of co-solvents for fast-charging lithium-ion cells. J. Electrochem. Soc. **165**, A2365-A2373 (2018).

16. Isken, P. et al. High flash point electrolyte for use in lithium-ion batteries. Electrochim. Acta **56**, 7530–7535 (2011).

17. Wang, Q., Zakeeruddin, S. M., Exnar, I. & Gratzel, M. 3-methoxypropionitrile-based novel electrolytes for high-power Li-ion batteries with nanocrystalline Li$_4$Ti$_5$O$_{12}$ anode. J. Electrochem. Soc. **151**, A1598-A1603 (2004).

18. Cho, Y.-G., Kim, Y.-S., Sung, D.-G., Seo, M.-S. & Song, H.-K. Nitrile-assistant eutectic electrolytes for cryogenic operation of lithium ion batteries at fast charges and discharges. Energy Environ. Sci. **7**, 1737–1743 (2014).

19. Han, J.-G. et al. An electrolyte additive capable of scavenging HF and PF$_5$ enables fast charging of lithium-ion batteries in LiPF$_6$-based electrolytes. J. Power Sources **446**, 227366 (2020).

20. Hamenu, L. et al. Lithium-silica nanosalt as a low-temperature electrolyte additive for lithium-ion batteries. Curr. Appl. Phys. **16**, 611–617 (2016).

21. Li, Q. et al. Wide-temperature electrolytes for lithium-ion batteries. ACS Appl. Mater. Interfaces **9**, 18826–18835 (2017).

22. Shi, J. et al. Improving the graphite/electrolyte interface in lithium-ion battery for fast charging and low temperature operation: Fluorosulfonyl isocyanate as electrolyte additive. J. Power Sources **429**, 67–74 (2019).

23. Xu, K. Nonaqueous liquid electrolytes for lithium-based rechargeable batteries. Chem. Rev. **104**, 4303–4417 (2004).

24. Yamada, Y., Yaegashi, M., Abe, T. & Yamada, A. A superconcentrated ether electrolyte for fast-charging Li-ion batteries. Chem. Commun. **49**, 11194–11196 (2013).

25. Yamada, Y. et al. Unusual stability of acetonitrile-based superconcentrated electrolytes for fast-charging lithium-ion batteries. J. Am. Chem. Soc. **136**, 5039–5046 (2014).

26. Nakanishi, A. et al. Sulfolane-based highly concentrated electrolytes of lithium bis(trifluoromethanesulfonyl)amide: ionic transport, Li-ion coordination, and Li-S battery performance. J. Phys. Chem. C **123**, 14229–14238 (2019).

27. Jiang, L.-L. et al. Inhibiting solvent co-intercalation in a graphite anode by a localized high-concentration electrolyte in fast-charging batteries. Angew. Chem. Int. Ed. **60**, 3402–3406 (2021).

28. Zhang, X. et al. Advanced electrolytes for fast-charging high-voltage lithium-ion batteries in wide-temperature range. Adv. Energy Mater. **10**, 2000368 (2020).

29. Okoshi, M., Chou, C.-P. & Nakai, H. Theoretical analysis of carrier ion diffusion in superconcentrated electrolyte solutions for sodium-ion batteries. J. Phys. Chem. B **122**, 2600–2609 (2018).

30. Yamada, Y., Wang, J., Ko, S., Watanabe, E. & Yamada, A. Advances and issues in developing salt-concentrated battery electrolytes. Nat. Energy **4**, 269–280 (2019).

31. Borodin, O. et al. Liquid structure with nano-heterogeneity promotes cationic transport in concentrated electrolytes. ACS Nano **11**, 10462–10471 (2017).

32. Zheng, J., Lochala, J. A., Kwok, A., Deng, Z. D. & Xiao, J. Research progress towards understanding the unique interfaces between concentrated electrolytes and electrodes for energy storage applications. Adv. Sci. **4**, 1700032 (2017).

33. Xu, K., von Cresce, A. & Lee, U. Differentiating contributions to "ion transfer" barrier from interphasial resistance and Li$^+$ desolvation at electrolyte/graphite interface. Langmuir **26**, 11538–11543 (2010).

34. Takada, K. et al. Unusual passivation ability of superconcentrated electrolytes toward hard carbon negative electrodes in sodium-ion batteries. ACS Appl. Mater. Interfaces **9**, 33802–33809 (2017).

35. Yamada, Y. & Yamada, A. Superconcentrated electrolytes to create new interfacial chemistry in non-aqueous and aqueous rechargeable batteries. Chem. Lett. **46**, 1056–1064 (2017).

36. Yao, Y.-X. et al. Regulating interfacial chemistry in lithium-ion batteries by a weakly solvating electrolyte. Angew. Chem. Int. Ed. **60**, 4090–4097 (2021).

37. Zhao, Q. et al. Designing electrolytes with polymerlike glass-forming properties and fast ion transport at low temperatures. *Proc. Natl. Acad. Sci. U.S.A.* **117**, 26053–26060 (2020).

38. Xu, W., Welty, C., Peterson, M. R., Read, J. A. & Stadie, N. P. Exploring the limits of the rapid-charging performance of graphite as the anode in lithium-ion batteries. J. Electrochem. Soc. **169**, 010531 (2022).

39. Zhu, Y., Gao, T., Fan, X., Han, F. & Wang, C. Electrochemical techniques for intercalation electrode materials in rechargeable batteries. Acc. Chem. Res. **50**, 1022–1031 (2017).

40. Fan, X. et al. High energy-density and reversibility of iron fluoride cathode enabled via an intercalation-extrusion reaction. Nat. Commun. **9**, 2324 (2018).

41. Fan, X. et al. Pomegranate-structured conversion-reaction cathode with a built-in Li source for high-energy Li-ion batteries. ACS Nano **10**, 5567–5577 (2016).

42. Zhang, S. S., Xu, K. & Jow, T. R. Electrochemical impedance study on the low temperature of Li-ion batteries. Electrochim. Acta **49**, 1057–1061 (2004).

43. Lindstrom, H. et al. Li^+ ion insertion in TiO_2 (anatase).2. voltammetry on nanoporous films. J. Phys. Chem. B **101**, 7717–7722 (1997).

44. Chen, J. et al. Intercalation of Bi nanoparticles into graphite results in an ultra-fast and ultra-stable anode material for sodium-ion batteries. Energy Environ. Sci. **11**, 1218–1225 (2018).

45. Dong, X. et al. Environmentally-friendly aqueous Li (or Na)-ion battery with fast electrode kinetics and super-long life. Sci. Adv. **2**, e1501038 (2016).

46. Liu, H. et al. A disordered rock salt anode for fast-charging lithium-ion batteries. Nature **585**, 63–67 (2020).

47. Choi, S., Kwon, T.-W., Coskun, A. & Choi, J. W. Highly elastic binders integrating polyrotaxanes for silicon microparticle anodes in lithium ion batteries. Science **357**, 279–283 (2017).

48. Markevich, E., Salitra, G., Chesneau, F., Schmidt, M. & Aurbach, D. Very stable lithium metal stripping-plating at a high rate and high areal capacity in fluoroethylene carbonate-based organic electrolyte solution. ACS Energy Lett. **2**, 1321–1326 (2017).

49. Chen, J. et al. Electrolyte design for LiF-rich solid-electrolyte interfaces to enable high-performance microsized alloy anodes for batteries. Nat. Energy **5**, 386–397 (2020).

50. Fan, X. et al. Fluorinated solid electrolyte interphase enables highly reversible solid-state Li metal battery. Sci. Adv. **4**, eaau9245 (2018).

51. Li, Y. et al. Atomic structure of sensitive battery materials and Interfaces revealed by cryo-electron microscopy. Science **358**, 506–510 (2017).

52. Zachman, M. J., Tu, Z., Choudhury, S., Archer, L. A. & Kourkoutis, L. F. Cryo-STEM mapping of solid-liquid interfaces and dendrites in lithium-metal batteries. Nature **560**, 345-+ (2018).

53. Han, B. et al. Additive stabilization of SEI on graphite observed using cryo-electron microscopy. Energy Environ. Sci. **14**, 4882–4889 (2021).

54. Mao, C., Ruther, R. E., Li, J., Du, Z. & Belharouak, I. Identifying the limiting electrode in lithium ion batteries for extreme fast charging. Electrochem. Commun. **97**, 37–41 (2018).

55. Yang, X.-G. & Wang, C.-Y. Understanding the trilemma of fast charging, energy density and cycle life of lithium-ion batteries. J. Power Sources **402**, 489–498 (2018).

56. Zhang, S. S. Unveiling capacity degradation mechanism of Li-ion battery in fast-charging process. Chemelectrochem **7**, 555–560 (2020).

57. Fan, X. et al. All-temperature batteries enabled by fluorinated electrolytes with non-polar solvents. Nat. Energy **4**, 882–890 (2019).

58. Plichta, E. J. & Behl, W. K. A low-temperature electrolyte for lithium and lithium-ion batteries. J. Power Sources **88**, 192–196 (2000).

59. Aurbach, D. et al. Review on electrode-electrolyte solution interactions, related to cathode materials for Li-ion batteries. J. Power Sources **165**, 491–499 (2007).

60. Nie, Z., Liu, Y., Yang, L., Li, S. & Pan, F. Construction and application of materials knowledge graph based on author disambiguation: revisiting the evolution of $LiFePO_4$. Adv. Energy Mater. **11**, 2003580

(2021).

61. Uhlmann, C., Illig, J., Ender, M., Schuster, R. & Ivers-Tiffee, E. In situ detection of lithium metal plating on graphite in experimental cells. J. Power Sources **279**, 428–438 (2015).

62. Pidaparthy, S., Rodrigues, M.-T. F., Zuo, J.-M. & Abraham, D. P. Increased disorder at graphite particle edges revealed by multi-length scale characterization of anodes from fast-charged lithium-ion cells. J. Electrochem. Soc. **168**, 100509 (2021).

63. Heenan, T. M. M. et al. Identifying the origins of microstructural defects such as cracking within Ni-rich NMC811 cathode particles for lithium-ion batteries. Adv. Energy Mater. **10**, 2002655 (2020).

64. Fan, X. et al. Non-flammable electrolyte enables Li-metal batteries with aggressive cathode chemistries. Nat. Nanotechnol. **13**, 715–722 (2018).

65. Shimizu, K., Almantariotis, D., Gomes, M. F. C., Padua, A. A. H. & Lopes, J. N. C. Molecular force feld for ionic liquids V: hydroxyethylimidazolium, dimethoxy-2-methylimidazolium, and fluoroalkylimidazolium cations and bis(fluorosulfonyl)amide, perfluoroalkanesulfonylamide, and fluoroalkylfluorophosphate anions. J. Phys. Chem. B **114**, 3592–3600 (2010).

66. Sambasivarao, S. V. & Acevedo, O. Development of OPLS-AA force field parameters for 68 unique ionic liquids. J. Chem. Theory Comput. **5**, 1038–1050 (2009).
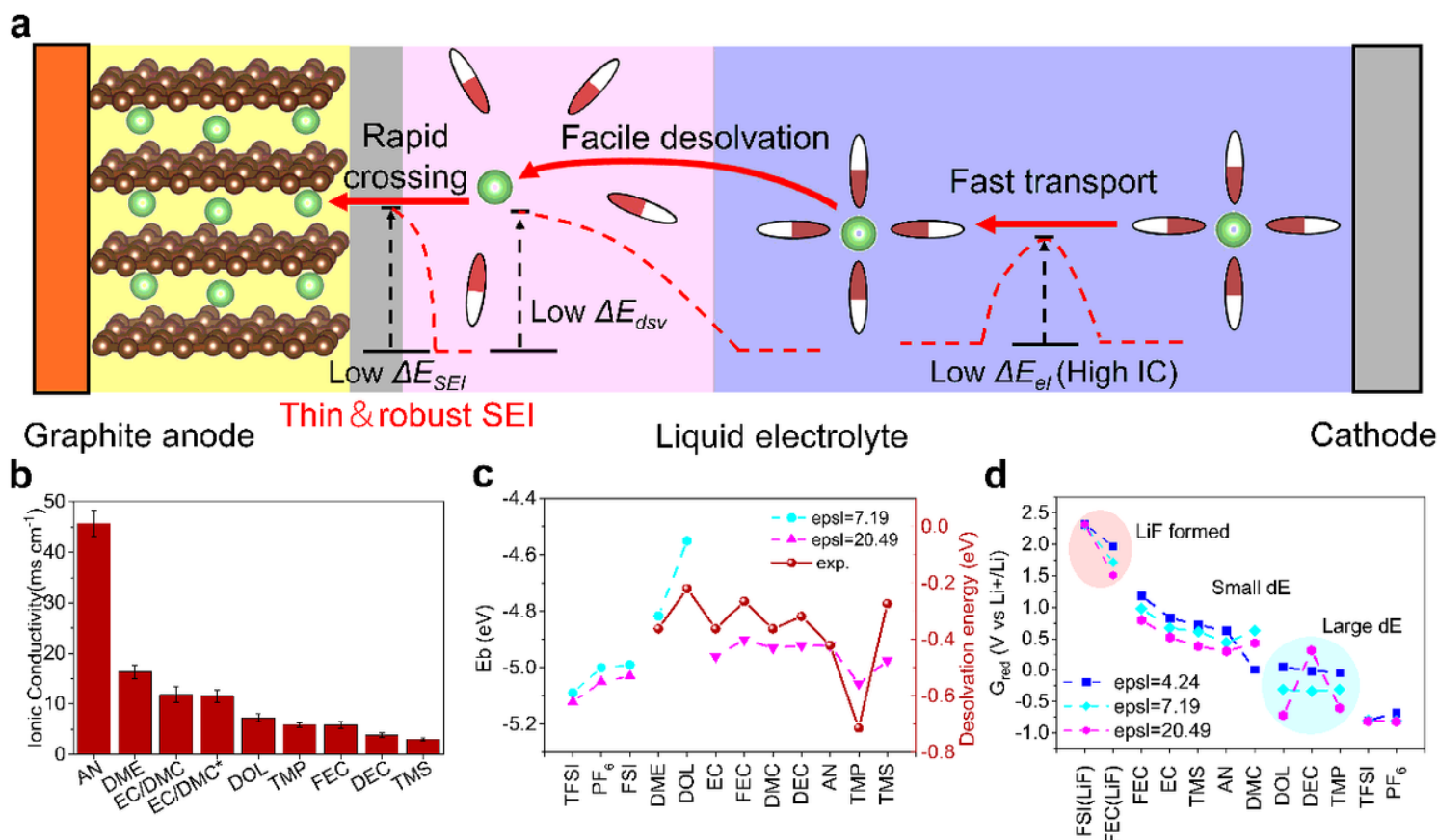
Figures

Figure 1

Design principles and solvation structures of the electrolytes. **a,** Schematic of fast-charging for the graphite anode considering all steps that the electrolyte affects Li$^+$ transport from cathode to anode during charging. **b,** Measured ionic conductivities of 1.0 m LiFSI in different solvents. EC/DMC* means the conventional electrolyte. **c,** Quantum chemistry calculated binding energies and measured desolvation energies. **d,** Calculated reduction potentials for anions and solvents using M05-2X/6-31++G(d, p).
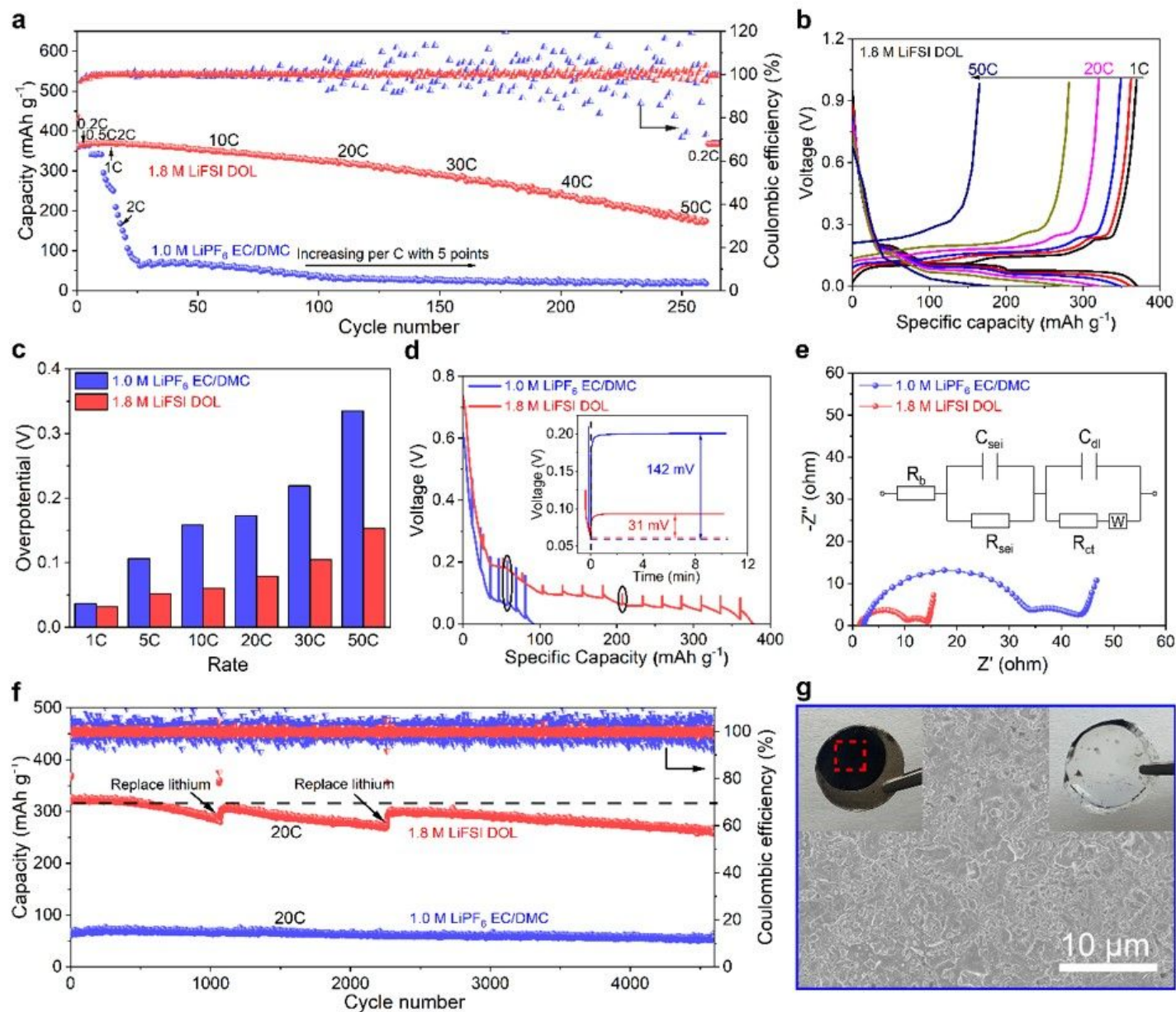
Figure 2

Electrochemical performance of graphite anodes in half cells. **a,** Rate performance of NG||Li cells with 1.8 M LiFSI DOL and 1.0 M LiPF$_6$ EC/DMC (1:1 by vol.). **b,** The corresponding charge/discharge curves of NG||Li cells with 1.8 M LiFSI DOL. **c,** Evolution of the overpotential at different rates of graphite electrode in two electrolytes. **d,** Discharge-voltage profiles of NG||Li cells via GITT measurements at 10C. The inset

showed voltage relaxation process during the rest taken from the black ellipses. **e, f,** Impedance spectra (e) and long-cycling performance at 20C (f) of NG||Li cells with two electrolytes. The rates of charge and discharge are the same for each cycle. **g,** Top-viewed SEM image of the Li metal electrode after 1100 cycles. The insets showed photographs of the Li metal electrode and separator after 1100 cycles. The SEM image was taken from the dotted boxes.
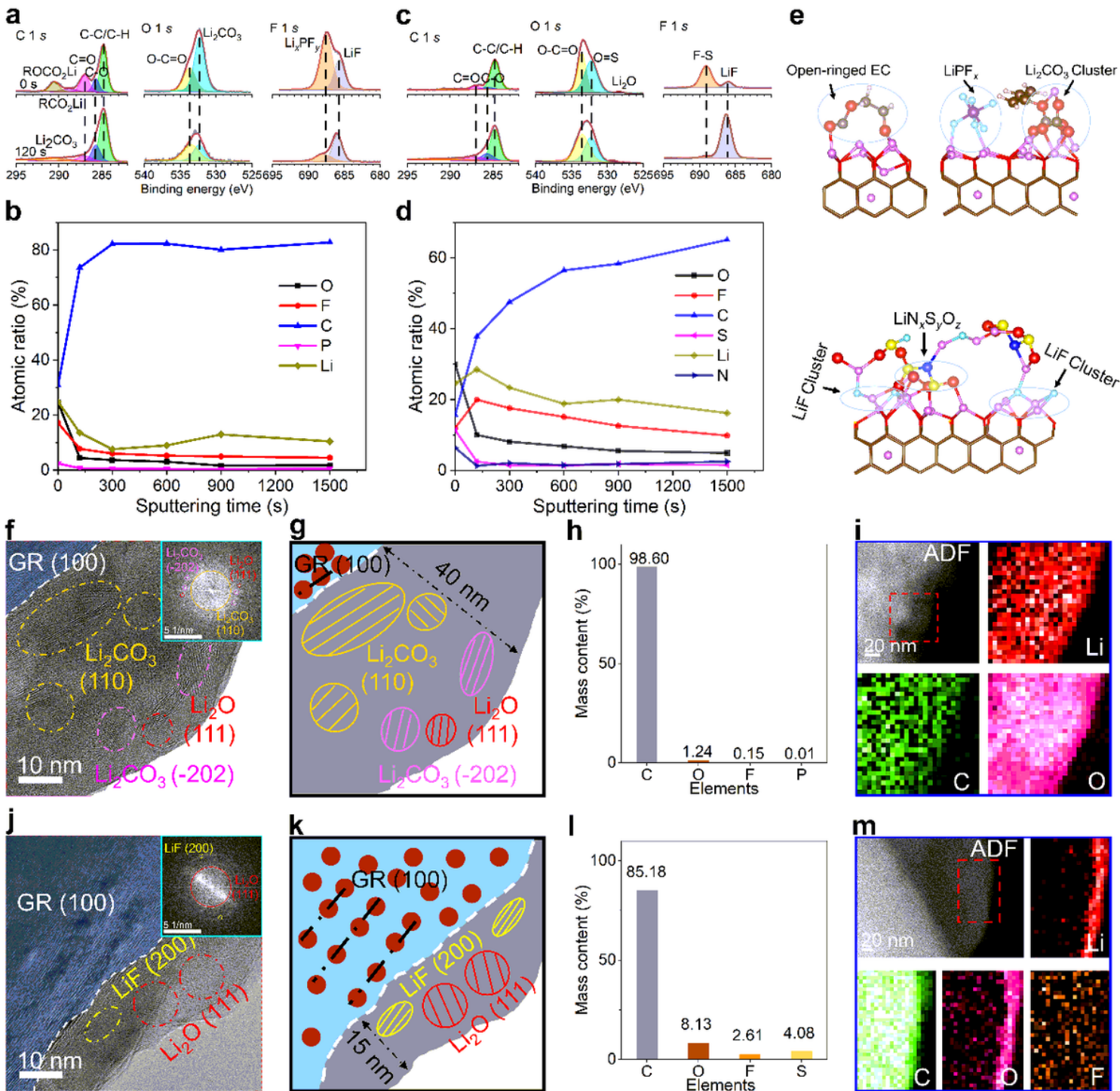

Figure 3

Characterization of the SEI on cycled graphite anodes. a, c, XPS spectra of the SEI formed on graphite electrodes with carbonate electrolyte **(a)** and 1.8 M LiFSI DOL **(c)**. The C 1s, O 1s and F 1s spectra were displayed after Ar$^+$-sputtering for 0 s and 120 s. **b, d,** Elemental contents of the SEI on graphite anodes cycled in carbonate electrolyte **(b)** and 1.8 M LiFSI DOL **(d)**. **e,** AIMD simulated atomic SEI structure between graphite and electrolytes. (Color code: Li, pink, P, purple, F, cany, C, brown, O, red, N, blue, S, yellow, graphite, brown wireframe). **f, j,** High-resolution cryo-TEM images of SEI films formed in carbonate electrolyte **(f)** and 1.8 M LiFSI DOL electrolyte **(j)**. Insets are the corresponding FFT pattern. **g, k,** The corresponding schematics of the two High-resolution cryo-TEM images. **h, l,** Different elemental mass content of the SEI films formed in carbonate electrolyte **(h)** and 1.8 M LiFSI DOL electrolyte **(l)**. **i, m,** High-resolution ADF STEM and EELS results of the graphite surface in carbonate electrolyte **(i)** and 1.8 M LiFSI DOL electrolyte **(m)**.
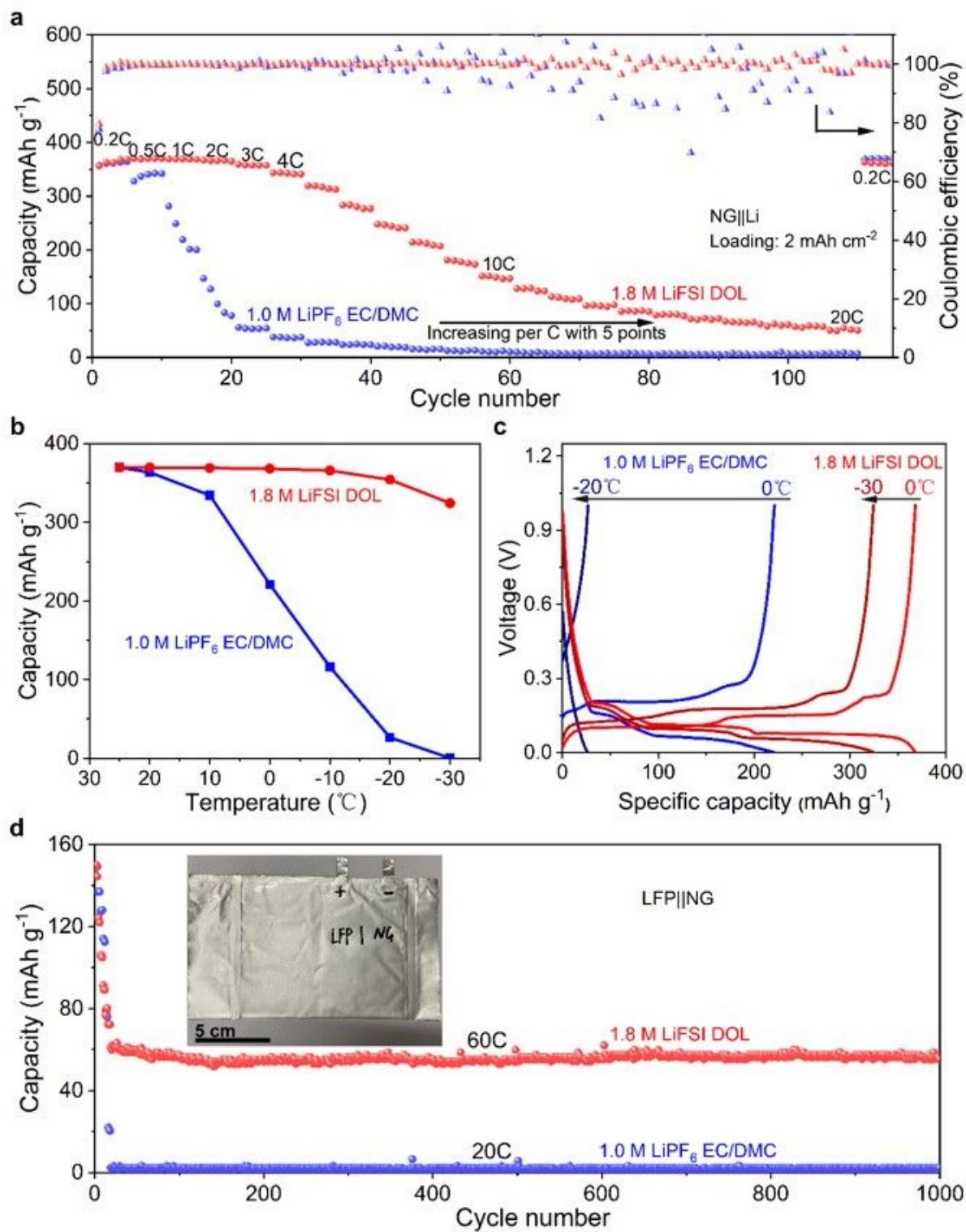
Figure 4

Electrochemical performances of cells under practical conditions. a, b, c, Rate (a), low temperature performances (b) and their corresponding charge/discharge curves (c) of NG||Li cells with two electrolytes. The loadings of graphite anodes are 2 mAh cm^{-2}. Same rates of charge/discharge for each cycle. d, Long cycling performance of LFP||NG pouch cells with two electrolytes. The inset shows a photograph of the LFP||NG pouch cell.
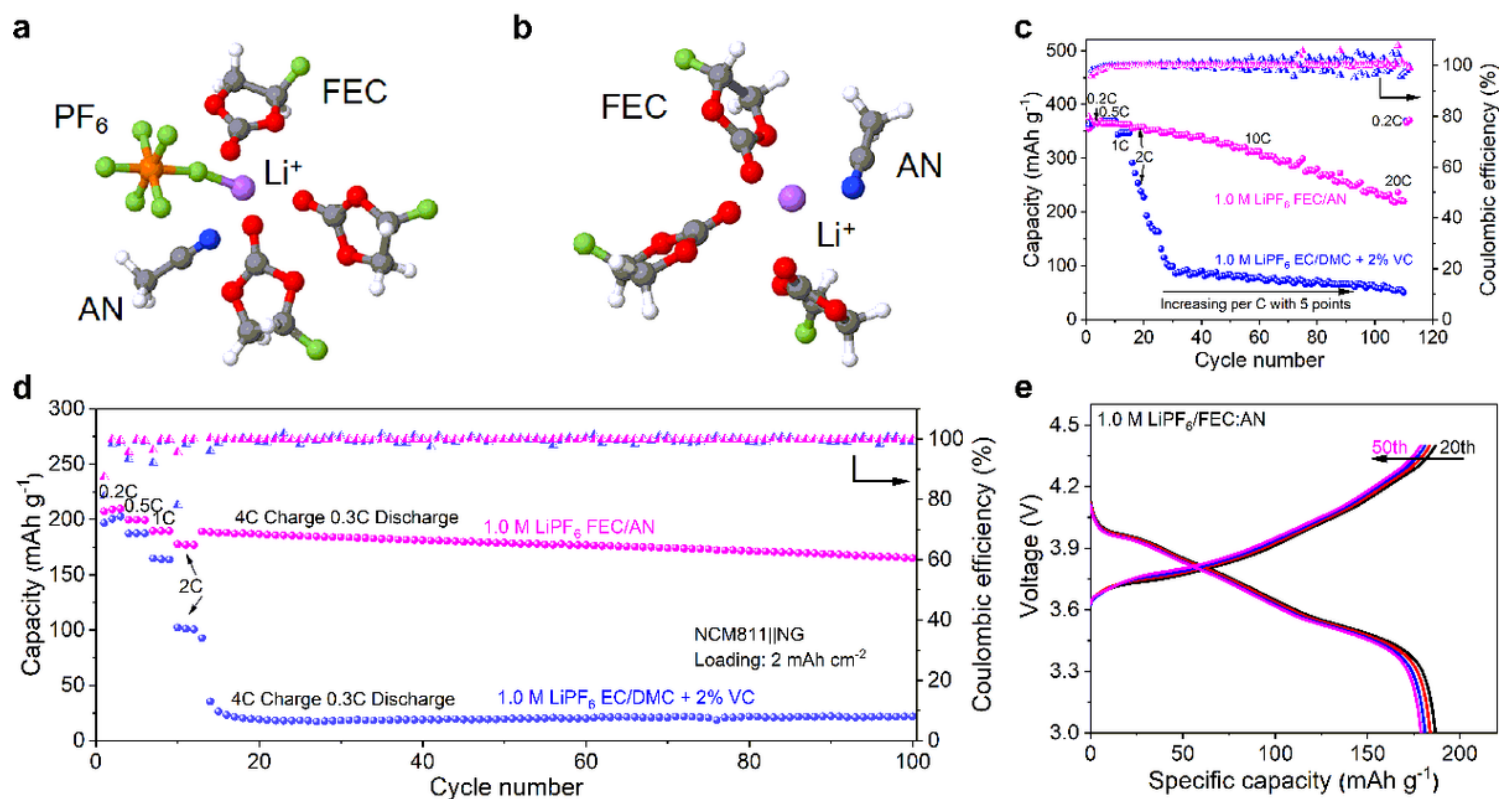
Figure 5

Solvation structures of the high-voltage electrolyte and the battery performance. **a**, **b**, Representative Li$^+$ solvation structures for the 1.0 M LiPF$_6$ FEC/AN electrolyte **(a)** with anion and **(b)** without anion. **c**, **d**, **e**, Rate performance **(c)** of NG||Li cells, long-cycling performance **(d)** at a tough condition (4C charge 0.3C discharge) and the corresponding charge/discharge curves **(e)** of NCM811||NG cells with 1.0 M LiPF$_6$ FEC/AN. The loading of active material is 2 mAh cm^{-2} in NCM811||NG cells. The N/P ratio is fixed at 1.

Supplementary Files

This is a list of supplementary files associated with this preprint. Click to download.

- SupplementaryMaterials.docx